Molyneux, SJ, Smit, R, Schaerer, D, Bouwens, RJ, Bradley, L, Hodge, JA, Longmore, SN, Schouws, S, van der Werf, P, Zitrin, A and Phillips, S

Spectroscopic confirmation of a gravitationally lensed Lyman break galaxy at z[C II]= 6.827 using NOEMA

MNRAS 000, 1–9 (2021) Preprint 2 March 2022 Compiled using MNRAS LATEX style file v3.0

Spectroscopic confirmation of a gravitationally lensed Lyman break galaxy at $z_{[CII]}$= 6.827 using NOEMA

S. J. Molyneux[1,2,★] R. Smit[1], D. Schaerer[3,4], R. J. Bouwens[5], L. Bradley[6], J. A. Hodge[5], S. N. Longmore[1], S. Schouws[5], P. van der Werf[5], A. Zitrin[7], S. Phillips[1]

[1] *Astrophysics Research Institute, Liverpool John Moores University, 146 Brownlow Hill, Liverpool L3 5RF, UK*
[2] *European Southern Observatory, Karl-Schwarzschild-str. 2, 85748 Garching, Germany*
[3] *Observatoire de Genève, Université de Genève, 51 Ch. des Mail-lettes, 1290 Versoix, Switzerland*
[4] *CNRS, IRAP, 14 avenue E. Belin, 31400 Toulouse, France*
[5] *Leiden Observatory, Leiden University, NL-2300 RA Leiden, Netherlands*
[6] *Space Telescope Science Institute, Baltimore, MD 21218, USA*
[7] *Physics Department, Ben-Gurion University of the Negev, P.O. Box 653, Be'er-Sheva 8410501, Israel*

Accepted XXX. Received YYY; in original form ZZZ

ABSTRACT

We present the spectroscopic confirmation of the brightest known gravitationally lensed Lyman break galaxy in the Epoch of Reionisation, A1703-zD1, through the detection of [C II]158μm at a redshift of z = 6.8269 ± 0.0004. This source was selected behind the strong lensing cluster Abell 1703, with an intrinsic $L_{\rm UV} \sim L^*_{z=7}$ luminosity and a very blue *Spitzer*/IRAC [3.6]–[4.5] colour, implying high equivalent width line emission of [O III]+Hβ. [C II] is reliably detected at 6.1σ co-spatial with the rest-frame UV counterpart, showing similar spatial extent. Correcting for the lensing magnification, the [C II] luminosity in A1703-zD1 is broadly consistent with the local $L_{\rm [CII]}$ – SFR relation. We find a clear velocity gradient of 103 ± 22 km s^{-1} across the source which possibly indicates rotation or an ongoing merger. We furthermore present spectral scans with no detected [C II] above 4.6σ in two unlensed Lyman break galaxies in the EGS-CANDELS field at $z \sim 6.6 - 6.9$. This is the first time that NOEMA has been successfully used to observe [C II] in a 'normal' star-forming galaxy at $z > 6$, and our results demonstrate its capability to complement ALMA in confirming galaxies in the Epoch of Reionisation.

Key words: galaxies: evolution - galaxies: formation - galaxies: high-redshift

1 INTRODUCTION

In the past decade hundreds of galaxies have been identified in the Epoch of Reionisation (EoR), selected from their rest-frame UV light, using Hubble Space Telescope (*HST*) and ground-based optical/NIR observatories (Stark 2016, for a review and references therein). However, only a fraction of these sources have spectroscopic redshift determinations and we have a limited understanding of their physical properties. One reason for this is the difficulty in obtaining Lyman-α observations at such high redshifts, due to its absorption by neutral hydrogen in the intergalactic and interstellar medium (with detected Lyα emitters possibly residing in early ionised bubbles; e.g. Jung et al. 2020; Endsley et al. 2021).

In recent years ALMA has transformed this field by confirming the redshifts of galaxies out to redshift z = 9 (e.g., Smit et al. 2018; Hashimoto et al. 2018; Tamura et al. 2019; Hodge & da Cunha 2020; Bouwens et al. 2021) and providing the first view of their dust obscured star-formation (e.g., Watson et al. 2015; Laporte et al. 2017; Bowler et al. 2018; Schouws et al. 2021), the kinematics of these sources (e.g., Smit et al. 2018; Hashimoto et al. 2019; Fujimoto et al. 2019; Ginolfi et al. 2020), the cool gas traced by [C II] and highly ionised gas traced by [O III] (e.g., Maiolino et al. 2015; Inoue et al. 2016; Carniani et al. 2017; Laporte et al. 2017; Hashimoto et al. 2019; Tamura et al. 2019; Harikane et al. 2019; Bakx et al. 2020). Uncovering the physical properties of these primordial systems is fundamental to understanding the evolution of the first generation of galaxies and their role in Cosmic Reionisation.

In particular, ALMA has demonstrated its ability to detect [C II] in UV bright galaxies which are intrinsically bright (~2 – 3 × L^* at z = 7) at $z \gtrsim 5$ (Capak et al. 2015; Willott et al. 2015; Smit et al. 2018; Matthee et al. 2019; Béthermin et al. 2020; Bouwens et al. 2021). However, much less is known about galaxies at these high redshifts which are more representative of the galaxy population as a whole ($L \leq L^*_{z=7}$). Our best insights into this fainter population are rare, apparently bright sources, which have been gravitationally lensed (Knudsen et al. 2016; Bradač et al. 2017; Fujimoto et al. 2021; Laporte et al. 2021). Despite the capability of ALMA to probe galaxies in the EoR, it has limited sky coverage in the Northern Hemisphere and so interesting targets might be missed.

Recently, the Plateau de Bure Interferometer (PdBI) has been upgraded to the Northern Extended Millimeter Array (NOEMA). The upgrades have increased the number of antennae from 6 to 10 (with 2 more planned to eventually increase the total number to 12) providing more collecting power and therefore increased sensitivity to observe these fainter sources. A new correlator has also been installed (upgrading from Widex to PolyFix Schuster et al. 2018), which can

★ E-mail: s.j.molyneux@2019.ljmu.ac.uk

cover a larger frequency range in one setup, enabling faster line scans. These upgrades arguably make NOEMA the most powerful interferometer in the Northern Hemisphere, and therefore might play an important role in observing [C II] in galaxies at $z > 6$.

Here we report on a line search for [C II]158μm with NOEMA, targeting 3 galaxies in the Northern Hemisphere at $z \sim 6.6 - 6.9$. The targets have been selected from a larger sample of Lyman Break Galaxies, with high-precision photometric redshifts (Smit et al. 2014, 2015). A1703-zD1 is the standout target of our sample, lying behind the strong lensing cluster Abell 1703, with a magnification of ~9 (Bradley et al. 2012). Due to its exceptional observed brightness, it has been targeted many times with previous observations attempting to observe Lyα, C IV and C III with the Keck Observatory (Schenker et al. 2012; Stark et al. 2015; Mainali et al. 2018) and a previous attempt with PdBI (Schaerer et al. 2015) to observe [C II], however, these observations did not result in a significant detection.

In this paper we present the successful spectroscopic confirmation of A1703-zD1 and constraints on the properties of the other two sources based on their non-detections. The plan of the paper is as follows. In Section 2 we describe the sample selection and observations. In Section 3 we discuss the method for line scanning and the findings from our scans. In Section 4 we provide the properties of the sources and comparisons to the literature and in Section 5 we give our summary and conclusions. In this paper we adopt a Kroupa IMF (Kroupa 2001). We adopt $H_0 = 70\,\mathrm{km\,s^{-1}\,Mpc^{-1}}$, $\Omega_M = 0.3$, and $\Omega_\Lambda = 0.7$ throughout. Magnitudes are quoted in the AB system (Oke & Gunn 1983).

2 SAMPLE SELECTION AND OBSERVATIONS

2.1 Target selection and properties

We obtained NOEMA observations of three sources, A1703-zD1 (Bradley et al. 2012; Smit et al. 2014), EGS-5711424617 and EGS-1952445714 (hereafter EGS-5711 and EGS-1952 respectively; Smit et al. 2015). These galaxies were initially selected with the Lyman break technique as *HST*/F814W drop-out galaxies and subsequently identified as sources with blue *Spitzer*/IRAC [3.6]–[4.5] colours, implying high equivalent width [O III]+Hβ emission (Smit et al. 2014, 2015). The spectral energy distribution (SED) for each galaxy is shown in Appendix A.

We selected these targets due to their observed brightness ($m_{\mathrm{UV}} \sim 24 - 25$), but also as they are representative of 'normal' star-forming galaxies (SFR < 100 $\mathrm{M_\odot\ yr^{-1}}$) at $z \sim 7$, with intrinsic (corrected for lensing magnification, A1703-zD1 is magnified ~9×) UV SFRs of $5 - 38\ \mathrm{M_\odot\ yr^{-1}}$. A list of some of the basic properties for all three galaxies are shown in Table 1. These same selection criteria were recently used to successfully confirm galaxies with ALMA at $z_{[\mathrm{CII}]} = 6.808 - 6.854$ (Smit et al. 2018).

The inferred emission lines in the *Spitzer* observations reduce the probability range for the redshift such that observations can be carried out using one NOEMA setup. For both A1703-zD1 and EGS-1952 the photometric redshifts of $6.7^{+0.2}_{-0.1}$ and $6.75^{+0.11}_{-0.10}$, respectively, are within this range. However, we note that EGS-5711 has $z_{\mathrm{phot}} = 6.47^{+0.11}_{-0.10}$, outside of the colour selection range due to a tentative detection in the *HST*/F814W band. For the extreme emission line sources from (Smit et al. 2015), systematic changes in the estimated photometric redshift ($\Delta z \sim 1$) are found when making changes to the input template set (in particular the strength of the emission line equivalent widths of the templates) used to fit the SEDs. As a result of these systematic uncertainties, we rely on the Spitzer/IRAC colour selection from Smit et al. (2015) to identify sources most likely in the redshift range $z \sim 6.6 - 6.9$, which includes some cases (like EGS-5711) where the z_{phot} is not within this range.

For A1703-zD1 we use a magnification value of $9.0^{+0.9}_{-4.4}$ taken from Bradley et al. (2012) calculated using the model described in Zitrin et al. 2010. The magnification error represents the extreme value obtained from the minimum and maximum magnifications obtained within 0.5 arcsec of the target and assuming $\Delta z \pm 1.0$ for the source redshift. To obtain a better handle on the systematic uncertainties in the lensing magnification we ran two more trial models, one using a revised version of the Light Traces Mass (LTM) technique and one fully parametric model. These models suggest a magnification in agreement with that of Bradley et al. (2012) within the uncertainties, though towards the lower end ($\mu \sim 4 - 5$). Critically, the weight of the nearby cluster galaxy (seen in the bottom of Figure 1) is fixed according to the scaling relations, but in reality has a significant uncertainty that affects the magnification value. We therefore adopt the published magnification by Bradley et al. (2012) (μ=$9.0^{+0.9}_{-4.4}$), as the uncertainties are broad enough to include the new magnifications from the trial models.

Throughout the paper, we report measured quantities (i.e. [C II] flux) as observed in the image plane, without a magnification correction, whereas derived physical quantities (i.e. $L_{[\mathrm{CII}]}$, $\mathrm{SFR}_{[\mathrm{CII}]}$ and physical size) are corrected for the adopted lensing magnification.

2.2 NOEMA observations and data reduction

We obtained 1.2 mm observations using NOEMA in its most compact 10D configuration, with a single setup for each of the three sources, A1703-zD1, EGS-5711 and EGS-1952, approved in program W18FC.

Observations of A1703-zD1 were taken on 21 March 2019, with 4.1 hours on source, and covering the frequency range 241.45 – 249.08 GHz (upper side band, USB) and 225.97 – 233.60 GHz (lower side band, LSB), corresponding to a redshift range 6.63 – 6.87 and 7.14 – 7.41 respectively. The USB frequency range partly overlaps with PdBI observations taken in 2013 by Schaerer et al. (2015) and we combine the NOEMA and PdBI data in the *UV*-plane to obtain maximum depth over the redshift range of 6.80 – 6.88.

We observed EGS-5711 on 16 April, 30 April 2019 and 02 May with 7.1 hours on source in total. EGS-1952 was observed on 08 and 09 April 2019 as well as on 02 and 03 May 2019 with 8.7 hours on source in total. Observations for both of these targets covered the same frequency and redshift range. LSB coverage was 240.4 – 248.3 GHz, corresponding to redshift of 6.66 – 6.91 and USB coverage was 255.8 – 263.7 GHz, corresponding to redshift of 6.21 – 6.43. The coverage described here is shown alongside the SED in Appendix A.

All of the data were reduced using the GILDAS software. From the NOEMA data of A1703-zD1 alone, we obtain a datacube with a median rms of 0.87mJy in a 40 km $\mathrm{s^{-1}}$ channel, with a beam size of 1.52 × 1.28 arcsec. After merging with PdBI data (Schaerer et al. 2015) we obtain a datacube with a median rms of 0.83mJy in a 40 km $\mathrm{s^{-1}}$ channel, with a beam size of 1.57 × 1.31 arcsec (~ 2 times lower sensitivity than ALMA observations in Smit et al. 2018). We then tapered the datacube for A1703-zD1 such that the beam size matched the spatial extent of the source in the HST imaging using a 50 metre taper at a 170 degree angle, in order to obtain a more accurate measurement of the total flux. We also cleaned the data with 100 iterations before imaging the datacube, including a threshold of 0.85mJy (2 × rms) to reduce the effects of contamination from a strong CO(3-2) emission line signal observed from a serendipitous

Target ID	A1703-zD1	EGS-5711424617	EGS-1952445714
RA	13:14:59.418	14:19:57.114	14:19:19.524
DEC	+51:50:00.84	+52:52:46.17	+52:44:57.14
$z_{\rm phot}$	$6.7^{+0.2}_{-0.1}$ [a]	$6.47^{+0.11}_{-0.10}$ [b]	$6.75^{+0.11}_{-0.10}$ [b]
$m_{H_{160}}$	24.0 ± 0.1 [a]	25.1 ± 0.1[b]	25.3 ± 0.1[b]
$M_{\rm UV}$	−20.6 ± 0.5[c]	−21.77±0.10	−21.64±0.10
$\beta_{\rm UV}$	−1.56±0.32	−2.18±0.36	−2.36±0.43
μ	$9.0^{+0.9}_{-4.4}$ [a]	–	–

Table 1. Table of source properties based on previous observations. [a] Values from Bradley et al. (2012). [b] Values from Smit et al. (2015). [c] Values from Smit et al. (2014).

source. This leads to a median rms in the datacube of 0.73mJy in a 40 km s^{-1} channel, with a beam size of 2.88 × 1.48 arcsec.

We imaged the two EGS datacubes with natural weighting for optimal point source sensitivity, resulting in a beam size of 1.69 × 1.41 arcsec and 1.63 × 1.37 arcsec for EGS-5711 and EGS-1952 respectively. Our data reached a typical rms of 0.34 and 0.41 mJy in a 40 km s^{-1} channel respectively. We do not apply any tapering as our beam sizes are expected to cover any observable [C II] emission from these compact targets (Carniani et al. 2020).

We also produced continuum images using GILDAS for all three targets to provide constraints on the dust obscured star formation and on the dust content itself. For all three targets we merged the USB and LSB before making the continuum images. In the case of A1703-zD1 we removed the frequency range in which [C II] was detected in the corresponding side band. We find no continuum detections above 3σ within 1 arcsec of each source and therefore provide upper limits for the $L_{\rm IR}$ and SFR$_{\rm IR}$, presented in Table 2. These upper limits are derived by taking 3 × rms from the continuum image. Discussion about the significance of these continuum measurements can be found in Section 4.2.

We correct for any offset in the HST astrometry by identifying the closest star to the target galaxy in the Gaia Data Release 3 (DR3). For EGS-5711 and EGS-1952 the observations were taken ∼ 4 years apart and we correct for the proper motion of the star during that timeframe, before shifting our HST image to the Gaia reference star. Unfortunately for A1703-zD1, none of the stars present in the HST image had proper motion data from Gaia DR3 as a result of being too faint (G magnitudes > 21). Given that the HST imaging for Abell 1703 was taken in 2004 (>10 years apart from Gaia), and assuming a similar proper motion to the stars in the EGS field, we expect a ∼ 0.3 arcsec offset from the reported Gaia DR3 position due to proper motion. This angular distance is similar to the typical spatial offset found for the stars in the Abell 1703 field between the HST imaging and Gaia DR3 catalogue. As a result, no improvement in the astrometry of A1703-zD1 could be obtained and we relied on the original HST imaging (see Bradley et al. 2012), but note that a maximum 0.3 arcsec astrometrical offset between the HST and NOEMA data is possible. However, we point out that the morphology and size of the [C II] emission for A1703-zD1 matches well to the HST image, as shown in Figure 1, so any real offset is perhaps likely to be small. Further, the detection of a serendipitous source with much higher S/N is also present and is seen to be co-spatial with the host galaxy as shown in Figure D2.

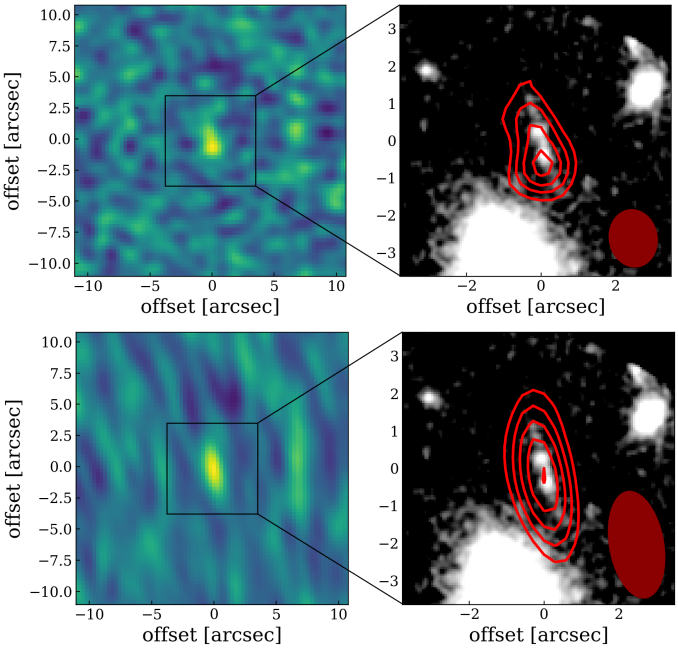

Figure 1. The detection of [C II] at z = 6.827 in A1703-zD1. The left panels show the NOEMA+PdBI data collapsed over the frequency range 242.76-242.86 GHz for the untapered (**top panels**) and tapered (**bottom panels**) imaging. The right panels show HST H_{160} imaging (grey-scale image) overlaid with the 2, 3, 4, 5 and 6 σ contours of the [C II] narrowband (red contours). The filled ellipses in the bottom right corner indicate the beam sizes (1.57 × 1.31 arcsec and 2.88 × 1.48 arcsec).

3 LINE SCANS

Using the datacubes we obtain after processing, we scan for prominent lines by collapsing channels in the range of 80-400 km s^{-1} (the range of expected [C II] line-widths). This optimises the width of the collapsed narrowband for which the strongest point-source signal within a 1 arcsec radius of the target source (identified in the *HST*-imaging) is found, if any. Scanning through the datacube also enables us to identify any lines present from serendipitous sources.

We replicate this scanning in the sign-inverse of the datacube, to check if any noise is comparable to the signal detected from the target source and assess the robustness of any tentative (>3σ) line detections. We extract spectra from identified line candidates by summing all pixels detected at S/N > 2 in the collapsed narrowband.

3.1 A1703-zD1

Taking our NOEMA observations of A1703-zD1 in isolation we find a signal at 242.90±0.01 GHz with S/N=4.6, co-spatial with the lower bright clump and extended along the lensed arc, visible in *HST*-imaging (See Figure 1). From previous observations by Schaerer et al. (2015), we independently identified a tentative detection of [C II] with S/N=3.4 at 242.853±0.009 GHz. The top panel of Figure 1 presents the line detection after combining both data-sets (see Section 2.2), collapsed in a 120 km s^{-1} channel centered on 242.8 GHz, with a peak S/N of 5.5. To obtain an unresolved measurement of A1703-zD1 we taper the datacube to match the spatial extent of A1703-zD1 (described in Section 2.2). From this we find a detection at 242.82±0.01 GHz with an increase in the peak S/N to 6.1, yielding a best-fit $z_{\rm [CII]}$ = 6.8269±0.0004 from the extracted spectrum (See

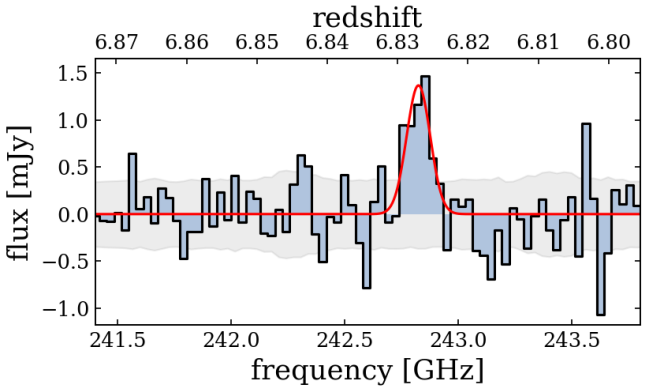

Figure 2. The spectrum of A1703-zD1 extracted by summing the flux over the source from all pixels with S/N>2, using the tapered imaging. The red line shows the best fit Gaussian line profile. The grey shaded region gives the measured rms throughout the spectrum.

Figure 2). This higher S/N when matching the spatial extent of the target (and alignment with the rest-frame UV emission) is a clear confirmation of the detection. We therefore use the tapered imaging for our final measurements. We collapse the datacube over the frequency range 242.72 – 242.92 GHz and measure the total flux using 2D gaussian fitting from the routine IMFIT in the Common Astronomy Software Application (CASA; McMullin et al. (2007)).

We also note that within the same datacube, we identify a serendipitous line signal at 241.59 GHz with S/N ∼ 14, (see spectrum in Fig D1) ∼ 8 arcsec offset to A1703-zD1. The signal is co-spatial with a foreground source (J131459.75+515008.6) which has $z_{\rm phot}$ ∼ 0.44 ± 0.11 (found in Sloan Digital Sky Survey DR12, Alam et al. 2015). We therefore identify the line as CO(3-2) (rest frame wavelength 867μm) at $z_{\rm spec}$ = 0.43127 ± 0.00003, consistent with the $z_{\rm phot}$. We also measure a 68μJy continuum flux from this source with S/N of 5.1.

3.2 EGS-5711 & EGS-1952

When scanning for [C II] in EGS-5711 we find a tentative signal with S/N = 4.6 at 246.16 ± 0.02 GHz, 0.5 arcsec away from the centre of the target. This line, if real, would put the source at z = 6.7263 ± 0.0006. A second signal at 242.10 ± 0.03 GHz with S/N = 3.4 is also found co-spatial with EGS-5711. The corresponding spectra and contour overlay plots for the S/N = 4.6 signal can be found in the appendix; figures B1 and B2. In figures C1 and C2 in the appendix we also present the spectra at the location of the source to illustrate the lack of detection there. Performing the same scan on the inverse datacube (searching within a radius of 15 arcsec), we find several signals with equivalent or higher S/N, the highest of which is S/N = 5.3. Given our 15 times larger search area, we expect ∼1 spurious signal above 4.5σ within 1 arcsec radius of our target. More observations are therefore required to confirm any detection.

For EGS-1952 we find no evidence for [C II] with S/N>3, co-spatial with the source. Spectra at the location of the source can be found in the appendix (Figures C3, C4.) Further, we find no continuum signal for both EGS-5711 and EGS-1952 and as a result, we only provide upper limits for the continuum flux and an upper limit estimate for the [C II] line flux, based on the spectral line obtained for A1703-zD1, scaled to the median rms of the EGS-5711 and EGS-1952 datacubes.

We can either interpret these non-detections as faint [C II] lines due to the low dust content of these sources or alternatively it is possible that the limited frequency range that was scanned for each object missed the line emission entirely. Deeper and wider scans would be needed to distinguish between these two interpretations (see Appendix A).

Target ID	A1703-zD1	EGS-5711	EGS-1952
$z_{\rm [CII]}$	6.8269±0.0004	–	–
S/N	6.1	–	–
[C II] flux (Jy km s^{-1})	0.28±0.06	< 0.17^{a}	< 0.21^{a}
FWHM$_{\rm [CII]}$ (km s^{-1})	155±31	–	–
Continuum flux (μJy)	< 24.5^{a}	< 27.4^{a}	< 28.7^{a}
$L_{\rm [CII]}$ (10^8 $L_\odot$)	0.35±0.07 ($^{+0.29}_{-0.04}$)^{c}	< 1.8^{a}	< 2.3^{a}
SFR$_{\rm [CII]}$ ($M_\odot$ yr^{-1})	4.3±0.9 ($^{+0.29}_{-0.04}$)^{c}	< 23.9^{a}	< 29.5^{a}
$L_{\rm UV}$ (10^{11} $L_\odot$)	0.39±0.04 ($^{+0.41}_{-0.04}$)^{c}	1.2±0.1	1.0±0.1
SFR$_{\rm UV}$ ($M_\odot$ yr^{-1})	6.7±0.6 ($^{+6.41}_{-0.61}$)^{c}	20.2±1.9	17.9±1.7
$L_{\rm IR}$ (10^{11} $L_\odot$)	< 0.35 (< 0.68)^{a,b,c}	< 3.6^{a,b}	< 3.9^{a,b}
SFR$_{\rm IR}$ ($M_\odot$ yr^{-1})	< 5.2 (< 10.1)^{a,b,c}	< 53.2^{a,b}	< 57.7^{a,b}
log(IRX)	< −0.05^{a}	< 0.48^{a}	< 0.57^{a}

Table 2. Galaxy Properties $^{a}3\sigma$ upper limits, ^{b}assuming a grey body approximation with T = 50K and β = 1.5, ^{c}corrected for a magnification of μ=9.0 (the uncertainty due to the lensing magnification are also shown in brackets). Observed quantities are uncorrected for magnification, while the derived physical properties use the magnification correction.

4 SOURCE PROPERTIES

Here we present the physical properties of our three targets derived from our observations and comparisons to the literature. A full table of galaxy properties is shown in Table 2.

4.1 $L_{\rm [CII]}$ vs SFR relation

In Figure 3 we present the measured [C II] luminosity as a function of SFR$_{\rm UV}$ and include sources from the literature for comparison (Matthee et al. 2019; Knudsen et al. 2016; Bradač et al. 2017; Fujimoto et al. 2021). The UV SFRs are calculated using the Kennicutt & Evans (2012) conversion, using a Kroupa IMF. EGS-5711 and EGS-1952 are given as 3σ upper limits.

In the local universe we see a tight $L_{\rm [CII]}$ – SFR relationship as shown by the De Looze et al. 2014 relation (log SFR = – 6.99 + 1.01 × log [CII]) in Figure 3. Recent studies of 'normal' (i.e. main sequence) star-forming galaxies with redshifts at 4.4 < z < 5.9 and galaxies at z∼6.5 with high Lyα luminositites have also shown consistency with the local relation when including the dust-obscured SFR (e.g., Matthee et al. 2019; Schaerer et al. 2020). In contrast, a few studies have found that lensed galaxies with a lower SFR are more likely to be below the locally observed relation (e.g., Knudsen et al. 2016; Bradač et al. 2017). In particularly the strongest lensed object, MS0451-H (Knudsen et al. 2016), with the lowest intrinsic SFR shows the strongest deficit in $L_{\rm [CII]}$. If confirmed, this could suggest differing ISM properties in faint, and possibly more metal-poor, high-redshift galaxies. A1703-zD1 is a strongly lensed galaxy with a modest intrinsic SFR$_{\rm UV}$ of 6.7 ± 0.6 M$_\odot$ yr^{-1}, but we find no evidence of a significant offset to the local relation, as A1703-zD1 lies slightly below, but still within 1σ of, the local $L_{\rm [CII]}$ – SFR

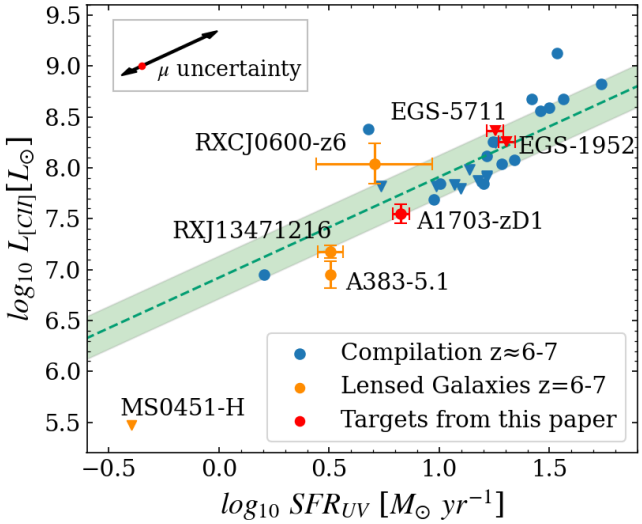

Figure 3. The [C II] line luminosity as a function of the star-formation rate, derived from the ultraviolet luminosity. The locally observed De Looze et al. 2014 relation is indicated by the dotted green line with the errors shown by the green shaded region. Sources with 3σ upper limits are shown by downward triangles. Our three targets are presented as red points. The black arrows in the top left indicate the magnification uncertainty for A1703-zD1. Changes in magnification affect both $L_{[CII]}$ and SFR_{UV}, such that A1703-zD1 moves along the local relation. We use a compilation of $z \approx 6-7$ sources for comparison (compiled from Matthee et al. 2019), shown in blue. In orange we highlight four lensed sources from the literature (Knudsen et al. 2016; Bradač et al. 2017; Fujimoto et al. 2021) for which three show an apparent offset from the local $L_{[CII]}$ – SFR relation, one of which shows a very clear offset (MS0451-H, discussed more in Section 4.1).

relation. We also note that including the magnification uncertainties in the calculations of $L_{[CII]}$ and $SFR_{[CII]}$ has no impact on the offset to the local relation as indicated by the arrows in Figure 3. However, including the 3σ upper-limit on the SFR_{IR} would place A1703-zD1 below the local relation.

An important consideration in assessing a possible [C II] deficit is the potential for extended [C II] emission (e.g., Fujimoto et al. 2019, 2020) compared to the rest-frame UV data, in particular for sources with smearing due to strong gravitational lensing. This effect was recently studied by Carniani et al. (2020), who find that [C II] emission can be two times more extended than [O III]. Specifically, Carniani et al. (2020) show that MS0451-H (Knudsen et al. 2016), nominally a 2.5σ deviation from the local De Looze relation (Figure 3), misses $\sim 60-80$ per cent of the [C II] emission if the effects of lensing are ignored. Taking into account possible extended [C II] moves MS0451-H to within 1σ of the local relation.

In A1703-zD1, we aim to account for lens smearing by tapering the datacube to match the spatial extent of A1703-zD1 in the *HST* imaging, allowing us to obtain a more accurate flux measurement. Without tapering and using the same routine as described in Section 3.1, we calculate a [C II] integrated flux value which is 51 per cent of our fiducial measurement. However, extended [C II] beyond the rest-frame UV could still be missed even with our current tapering strategy, consistent with Carniani et al. (2020).

4.2 L_{IR} and SFR_{IR} constraints

As discussed in Section 2.2, the continuum flux remains undetected for all our sources. We calculate upper limits for L_{IR} and SFR_{IR} by assuming an optically-thin grey-body infrared SED (Casey 2012) using T = 50K and β = 1.5, and present the results in Table 2. We estimate that these sources are likely below the classification of Luminous Infrared Galaxies (LIRG; $L_{IR} > 10^{11}\ L_\odot$). We furthermore find obscured SFR below 5-58 $M_\odot\ yr^{-1}$ (3σ limits), which suggests less than 44 – 74% of star-formation comes out in the IR, consistent with recent studies (e.g., Bowler et al. 2018; Schouws et al. 2021).

We derive UV slopes (β) and upper limits on the Infrared Excess ($IRX = L_{IR}/L_{UV}$) for all our targets (see Tables 1 and 2) and find that the upper-limits for EGS-5711 and EGS-1952 are consistent with either the Meurer et al. (1999) relation or a SMC-like dust attenuation.

However, given a moderately red UV slope for A1703-zD1 of $\beta \sim$ -1.56, we find this galaxy to be more consistent with an SMC like dust attenuation law, in agreement with stacking results of faint LBGs at $z \approx 2-10$ (Bouwens et al. 2016; Fudamoto et al. 2020, though see Schouws et al. 2021 for a discussion on the impact of the assumed dust temperature).

4.3 Velocity Structure

We use the spatial extent of the [C II] detection to investigate the velocity structure of A1703-zD1. We see a velocity gradient across A1703-zD1 shown in Figure 4. We find a maximum projected velocity difference over the galaxy (Δv_{obs}) of 103 ± 22 km s^{-1} from the first moment map. Such a velocity gradient could be the signature of a rotating disk, whilst another possibility is a merger of [C II] emitting galaxies. Similar velocity gradients are present in previous observations of high redshift galaxies (e.g., Smit et al. 2018; Hashimoto et al. 2019; Matthee et al. 2019; Fujimoto et al. 2021) as well as in simulations (Dekel & Burkert 2014).

To determine the likelihood of a disk-like rotation we compare the projected velocity range of a galaxy with the velocity dispersion of the system using $\Delta v_{obs}/2\sigma_{tot}$, where a ratio of >0.4 indicates a likely rotation dominated system (Förster Schreiber et al. 2009). We find $\Delta v_{obs}/2\sigma_{tot} = 0.79 \pm 0.23$ for A1703-zD1, which supports the interpretation of a possibly rotation dominated system. Bradley et al. (2012) find three distinct star-forming clumps with an extended linear morphology in the source-plane reconstruction of A1703-zD1. In Figure 4 we show the deflection due to the lensing magnification, using the LTM strong-lensing model published by Zitrin et al. (2010). This stretching of the source-plane leads to an effective increase in resolution of 3.5×, in the direction of the green arrow shown in Figure 4. The red and blue components identified in Figure 4 appear co-spatial with the two brightest clumps from Bradley et al. (2012). Clumps like this have been identified previously in high redshift galaxies and can be attributed to merging galaxies or large clumpy star formation due to the increased gas content in high-redshift galaxies. Higher resolution [C II] observations will be required to confirm a disk-like structure in A1703-zD1.

If we assume ordered circular rotation we can use the FWHM of [C II] to estimate the dynamical mass. We use $M_{dyn} = 1.16 \times 10^5 V_{cir}^2 D$ (Capak et al. 2015), where $V_{cir} = 1.763 \times \sigma_{[CII]} / \sin i$ in km s^{-1}, i is the disk inclination angle, and D is the disk diameter in kpc (we use D = 4 kpc found in Bradley et al. 2012; measured in the reconstructed sources-plane image). Assuming a viewing angle of 45 degrees we find $M_{dyn} = 12.1 \pm 4.8 \times 10^9\ M_\odot$. The stellar mass of A1703-zD1 was esimated to be $0.7 \pm 0.1 \times 10^9\ M_\odot$ (Bradley et al.

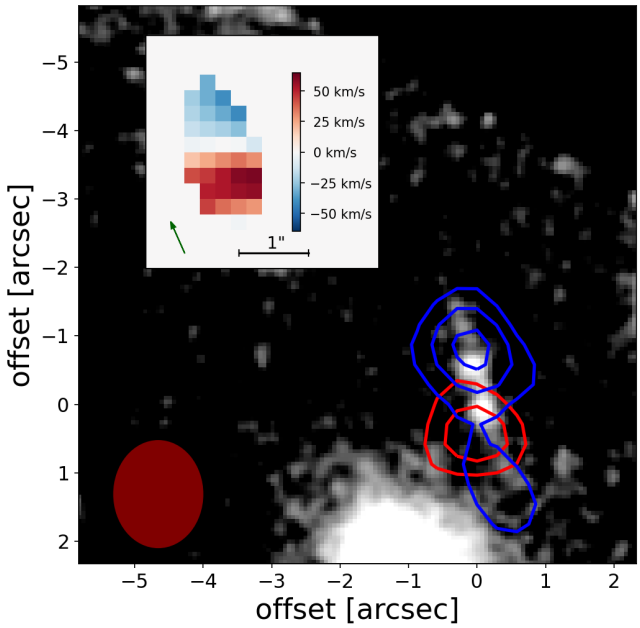

Figure 4. Main Panel: HST imaging overlaid with contours from the untapered datacube corresponding to 2,3 and 4σ [C II] emission collapsed over channels redwards (red contours) and bluewards (blue contours) of the measured line centre, showing evidence for a velocity gradient. The observations are spatially resolved, as shown by the filled ellipse indicating the beam size (1.57 × 1.31 arcsec). **Inset Panel:** First moment map of the detected [C II] from A1703-zD1 (showing pixels above 2σ). We measure a velocity difference over the galaxy of 103 ± 22 km s^{-1}. We show the green arrow to illustrate the stretching of the arc in the image plane with respect to the source-plane image of this source.

2012). This stellar mass is only ∼ 6 per cent of the total dynamical mass that we measure. This is somewhat low compared to dynamical measurements from Hα surveys at cosmic noon; for example, Stott et al. (2016) find a value of 22 ± 11 per cent in a sample of 584 z ∼ 1 galaxies and Wuyts et al. (2016) find a value of 32^{+8}_{-7} per cent in star forming galaxies 0.6 < z < 2.6. Larger and more detailed samples of dynamical measurements at $z \sim 7$ will be needed to establish evolutionary trends with redshift. We also note that there are large uncertainties on the dynamical mass, as there is a large dependency on the viewing angle (which is unknown). However, this low ratio does suggest that A1703-zD1 is a gas rich system, similar to typical star-forming galaxies 3 Gyr later in cosmic time.

5 SUMMARY AND CONCLUSIONS

We have presented new NOEMA observations, scanning for the [C II]158μm line in three Lyman break galaxies with photometric redshifts at $z = 6.6 - 6.9$. Our main findings are as follows:

- We detect [C II] in one of our three sources, confirming the redshift at $z = 6.8269 \pm 0.0004$ for the strongly lensed galaxy A1703-zD1 (6.1σ). Our non-detections are consistent with these being dust-poor galaxies with low [C II] luminosity.
- We carefully account for any extended emission of [C II] due to lens smearing in A1703-zD1 and find the [C II] luminosity to be consistent with, but slightly below, the local $L_{[CII]} - SFR$ relation.
- No continuum emission is detected in any of the three targeted sources, suggesting less than 44 – 74% of star-formation comes out in the IR. For A1703-zD1, our results are most consistent with an SMC attenuation curve.
- We see a velocity gradient across A1703-zD1, with a kinematic ratio that suggests a possible rotation dominated system, though higher resolution [C II] observations will be needed to confirm this.

Over the last few years ALMA has demonstrated its role as a "redshift machine" in the Epoch of Reionisation by confirming galaxies out to redshift $z = 9$. In this paper we have demonstrated the ability of NOEMA to search for [C II] in 'normal' star-forming galaxies at $z > 6$, complementing ALMA by observing EoR galaxies in the Northern Hemisphere, with [C II] as a reliable spectroscopic tracer of these distant systems. With the launch of JWST this capability will be particularly useful for rare, lensed sources and intrinsically luminous objects that will be discovered far outside the limited JWST survey area using the next generation of large area surveys, such as the Euclid mission and the Rubin observatory.

ACKNOWLEDGEMENTS

We thank the anonymous referee for their constructive feedback and useful suggestions. RS acknowledges support from a STFC Ernest Rutherford Fellowship (ST/S004831/1). AZ acknowledges support by Grant No. 2020750 from the United States-Israel Binational Science Foundation (BSF) and Grant No. 2109066 from the United States National Science Foundation (NSF), and by the Ministry of Science & Technology, Israel. JH gratefully acknowledges support of the VIDI research program with project number 639.042.611, which is (partly) financed by the Netherlands Organisation for Scientific Research (NWO).

DATA AVAILABILITY

The reduced data underlying this article will be shared on reasonable request to the corresponding author.

REFERENCES

Alam S., et al., 2015, ApJS, 219, 12
Bakx T. J. L. C., et al., 2020, MNRAS, 493, 4294
Béthermin M., et al., 2020, A&A, 643, A2
Bouwens R. J., et al., 2016, ApJ, 833, 72
Bouwens R. J., et al., 2021, arXiv e-prints, p. arXiv:2106.13719
Bowler R. A. A., Bourne N., Dunlop J. S., et al., 2018, MNRAS, 481, 1631
Bradač M., et al., 2017, ApJ, 836, L2
Bradley L. D., et al., 2012, ApJ, 747, 3
Brammer G. B., van Dokkum P. G., Coppi P., 2008, ApJ, 686, 1503
Capak P. L., et al., 2015, Nature, 522, 455
Carniani S., et al., 2017, A&A, 605, A42
Carniani S., et al., 2020, MNRAS, 499, 5136
Casey C. M., 2012, MNRAS, 425, 3094
De Looze I., et al., 2014, A&A, 568, A62
Dekel A., Burkert A., 2014, MNRAS, 438, 1870
Endsley R., Stark D. P., Charlot S., et al., 2021, MNRAS, 502, 6044
Förster Schreiber N. M., et al., 2009, ApJ, 706, 1364
Fudamoto Y., et al., 2020, A&A, 643, A4
Fujimoto S., et al., 2019, ApJ, 887, 107
Fujimoto S., et al., 2020, ApJ, 900, 1
Fujimoto S., et al., 2021, ApJ, 911, 99
Ginolfi M., et al., 2020, A&A, 633, A90
Harikane Y., et al., 2019, ApJ, 883, 142
Hashimoto T., et al., 2018, Nature, 557, 392

Hashimoto T., Inoue A. K., Tamura Y., et al., 2019, PASJ, 71, 109
Hodge J. A., da Cunha E., 2020, Royal Society Open Science, 7, 200556
Inoue A. K., et al., 2016, Science, 352, 1559
Jung I., et al., 2020, ApJ, 904, 144
Kennicutt R. C., Evans N. J., 2012, ARA&A, 50, 531
Knudsen K. K., Richard J., Kneib J.-P., et al., 2016, MNRAS, 462, L6
Kroupa P., 2001, MNRAS, 322, 231
Laporte N., Nakajima K., Ellis R. S., Zitrin A., Stark D. P., Mainali R., Roberts-Borsani G. W., 2017, ApJ, 851, 40
Laporte N., et al., 2021, MNRAS, 505, 4838
Mainali R., et al., 2018, MNRAS, 479, 1180
Maiolino R., et al., 2015, MNRAS, 452, 54
Matthee J., et al., 2019, ApJ, 881, 124
McMullin J. P., Waters B., Schiebel D., Young W., Golap K., 2007, in Shaw R. A., Hill F., Bell D. J., eds, Astronomical Society of the Pacific Conference Series Vol. 376, Astronomical Data Analysis Software and Systems XVI. p. 127
Meurer G. R., Heckman T. M., Calzetti D., 1999, ApJ, 521, 64
Oke J. B., Gunn J. E., 1983, ApJ, 266, 713
Schaerer D., Boone F., Zamojski M., et al., 2015, A&A, 574, A19
Schaerer D., et al., 2020, A&A, 643, A3
Schenker M. A., Stark D. P., Ellis R. S., et al., 2012, ApJ, 744, 179
Schouws S., et al., 2021, arXiv e-prints, p. arXiv:2105.12133
Schuster K. F., et al., 2018, in Ground-based and Airborne Telescopes VII. SPIE, https://doi.org/10.1117/12.2313489
Smit R., et al., 2014, ApJ, 784, 58
Smit R., et al., 2015, ApJ, 801, 122
Smit R., et al., 2018, Nature, 553, 178
Stark D. P., 2016, ARA&A, 54, 761
Stark D. P., et al., 2015, MNRAS, 454, 1393
Stott J. P., et al., 2016, MNRAS, 457, 1888
Tamura Y., et al., 2019, ApJ, 874, 27
Watson D., Christensen L., Knudsen K. K., Richard J., Gallazzi A., Michałowski M. J., 2015, Nature, 519, 327
Willott C. J., Carilli C. L., Wagg J., Wang R., 2015, ApJ, 807, 180
Wuyts S., et al., 2016, ApJ, 831, 149
Zitrin A., et al., 2010, MNRAS, 408, 1916

APPENDIX A: PHOTOMETRIC REDSHIFT COVERAGE

Here we present the SEDs for all three targets in this paper, alongside the photometric redshift probability distributions, redshift coverage of the observations and in the case of A1703-zD1, the measured $z_{[\mathrm{CII}]}$. The SED fitting was done using the software Easy and Accurate Zphot from Yale (EAZY; Brammer et al. (2008)), see Smit et al. (2015) for a full description.

We note that for EGS-5711, NOEMA did not cover the central z_{phot} of $6.47^{+0.11}_{-0.10}$. The systematic uncertainties in estimating photometric redshifts in extreme emission line galaxies are discussed in section 2.1, which motivated a line search at $z \sim 6.6-6.9$ based on the Smit et al. (2015) colour selection.

APPENDIX B: EGS-5711 TENTATIVE DETECTION

Here we present a 4.6σ signal for EGS-5711, with the contours overlayed on the HST imaging in Figure B1 and the corresponding spectra in Figure B2. The spectral extraction is the same as described in Section 3. The weak signal is very narrow and clearly offset from the HST target, which likely makes this a spurious detection.

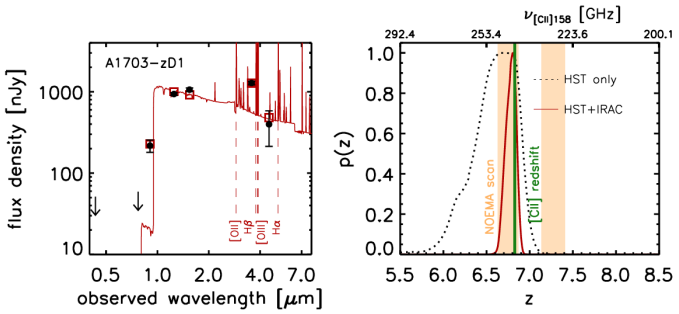

Figure A1. A1703-zD1 SED (**left panel**) and redshift probability distribution distribution (**right panel**). Coverage by the NOEMA sidebands (USB and LSB) is indicated by the shaded orange region. The dotted black line and solid red line represent the probability for the target to be at a certain redshift based on HST only and HST+IRAC data, respectively. Here the USB was selected to cover the peak probability in the photometric redshift range, which is indeed where the detection of [C II] was made, indicated by the solid green line.

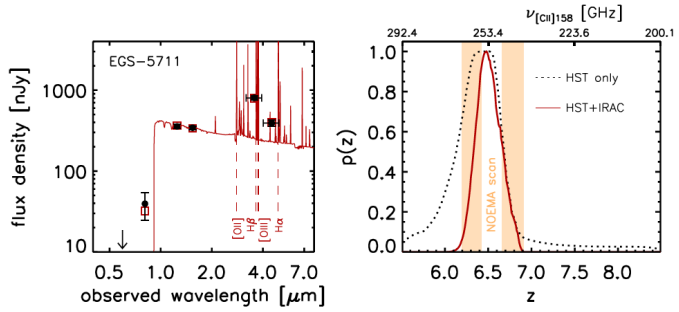

Figure A2. EGS-5711 SED (**left panel**) and redshift probability distribution distribution (**right panel**). Coverage by the NOEMA sidebands (USB and LSB) is indicated by the shaded orange region. The dotted black line and solid red line represent the probability for the target to be at a certain redshift based on HST only and HST+IRAC data, respectively. This target was selected to be at $z \sim 6.6-6.9$ based on HST+IRAC data colour criteria (Smit et al. 2015), however, the peak of the p(z) suggests a possible lower redshift. A broader and deeper line scan will be needed to establish the spectroscopic redshift of this source.

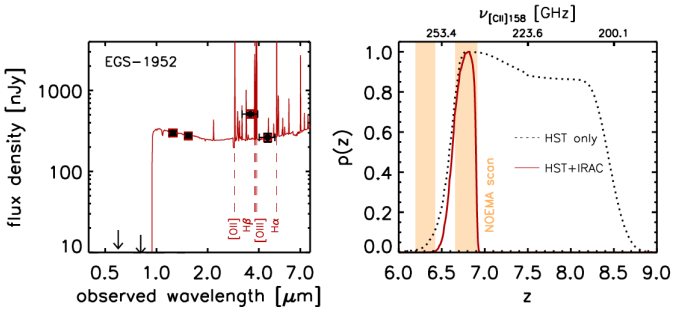

Figure A3. EGS-1952 SED (**left panel**) and redshift probability distribution (**right panel**). Coverage by the NOEMA sidebands (USB and LSB) is indicated by the shaded orange region. The dotted black line and solid red line represent the probability for the target to be at a certain redshift based on HST only and HST+IRAC data, respectively.

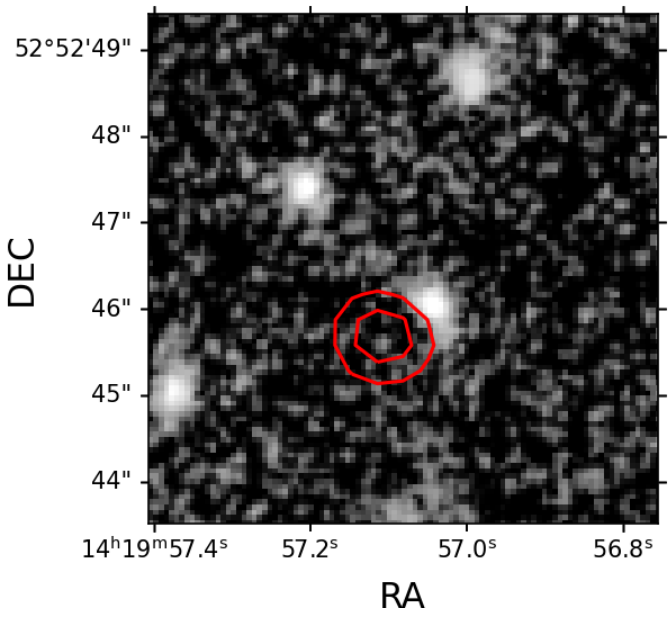

Figure B1. The S/N=4.6 signal found for EGS-5711. Background shows the HST H-band image with red contours corresponding to 3 and 4 σ [C II] emission. The extracted spectrum is also shown in Figure B2. This source would require further observations to confirm a robust detection.

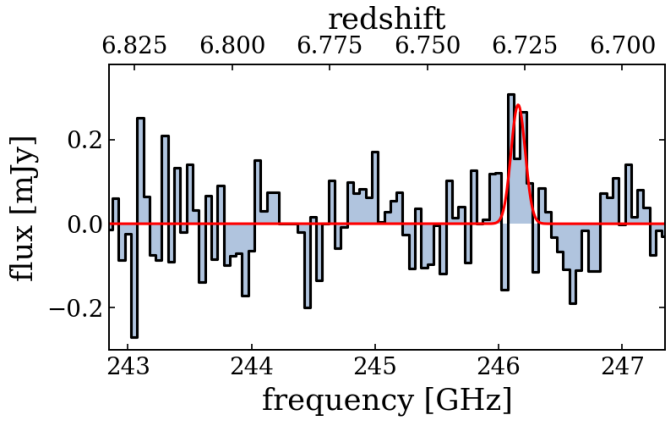

Figure B2. EGS-5711 spectrum of the S/N = 4.6 signal, extracted from the region of the contours shown in Figure B1, with the best-fit Gaussian line profile in red.

APPENDIX C: EMPTY SCANS

In Figures C1, C2, C3 and C4 we present the empty line scans in the LSB and USB for both EGS targets. The extractions were taken simply from the central pixel of the observations.

APPENDIX D: SERENDIPITOUS SOURCE IN A1703-ZD1 CUBE

Here we present a serendipitous 14σ detection in the datacube of A1703-zD1, with the spectra shown in D1 and the line contours overlayed on the HST imaging in D2. The spectral extraction is the same as described in Section 3. The detection is co-spatial with a fore-

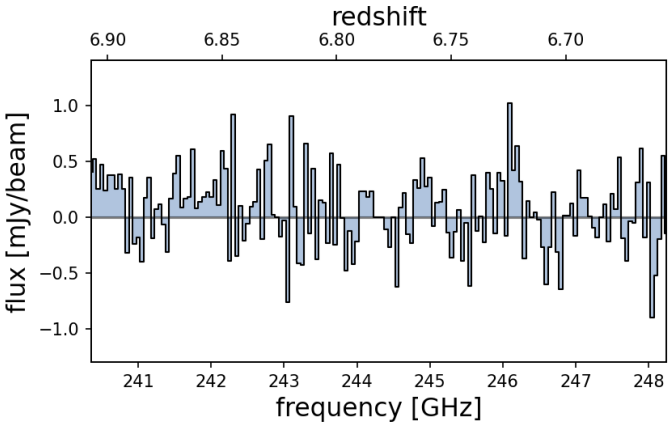

Figure C1. LSB spectra taken at the location of EGS-5711. We find no robust detection and present upper limits in table 2.

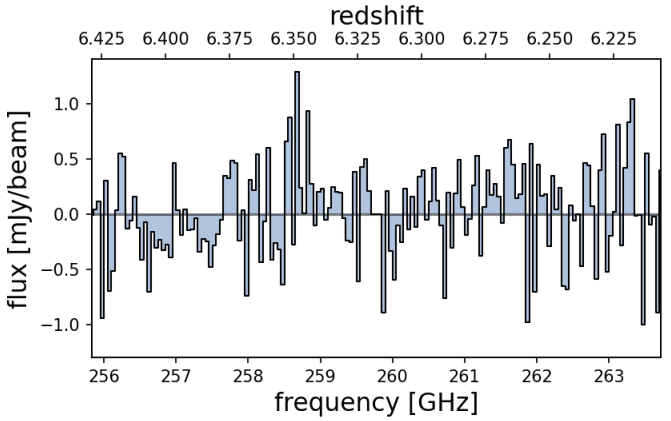

Figure C2. USB spectra taken at the location of EGS-5711.

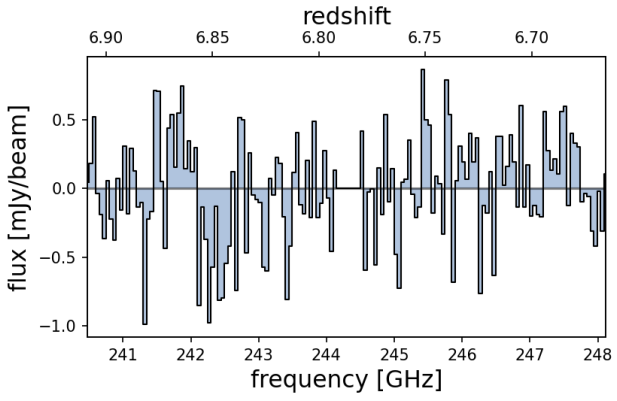

Figure C3. LSB spectra taken at the location of EGS-1952. We find no detection and present upper limits in table 2.

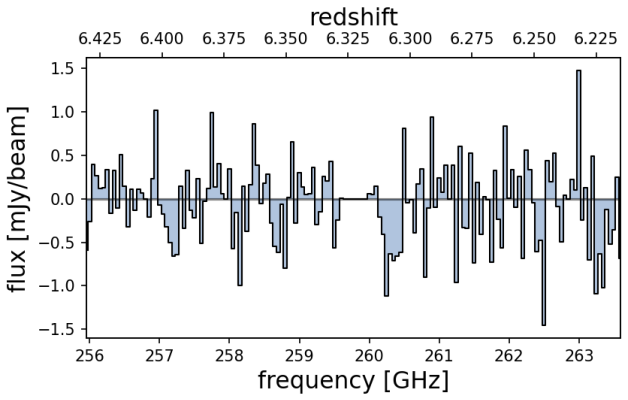

Figure C4. USB spectra taken at the location of EGS-1952.

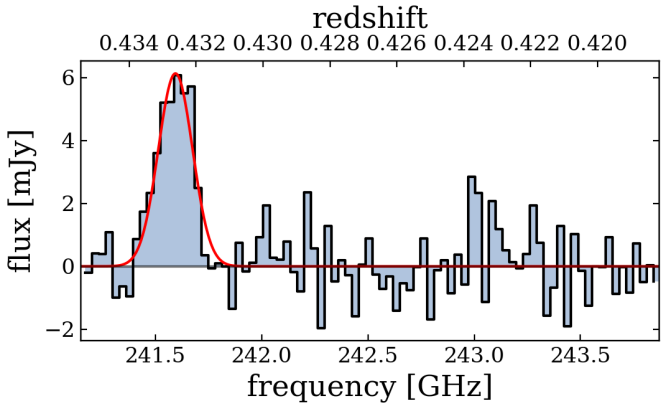

Figure D1. Spectrum of the serendipitous line identified in the datacube of A1703-zD1, with the best-fit Gaussian line profile in red. The redshifts plotted along the upper horizontal axis are based on the assumption the line detection is CO(3-2) for the source J131459.75+515008.6. The S/N of the line is 14.

ground source (J131459.75+515008.6) which has $z_{\rm phot}$ ~0.44 ± 0.11 (found in Sloan Digital Sky Survey DR12, Alam et al. 2015). We therefore attribute the line detection to CO(3-2) (rest frame wavelength 867μm) putting the source at $z_{\rm spec}$ = 0.43127 ± 0.00003, consistent with the $z_{\rm phot}$.

This paper has been typeset from a TEX/LATEX file prepared by the author.

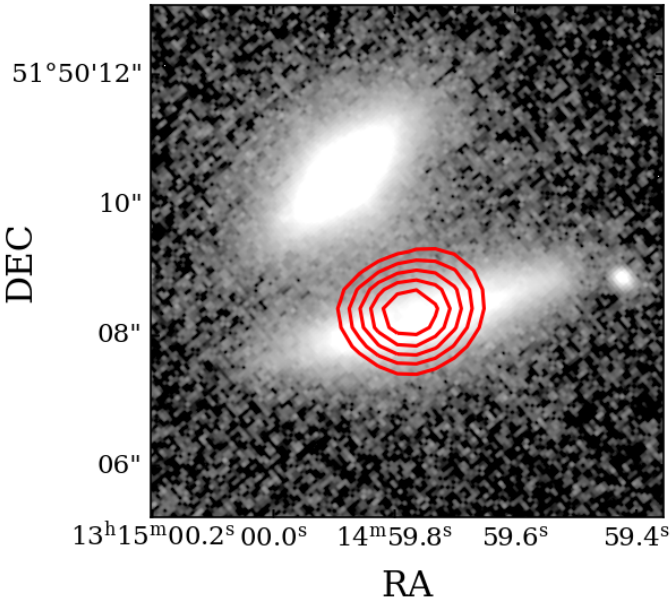

Figure D2. Serendipitous source (J131459.75+515008.6) with red contours overlayed corresponding to 4, 6, 8, 10 and 12 σ, identified as CO(3-2) emission. Background shows the HST z_{850} imaging of Abell 1703.